analytical chemistry

Article

pubs.acs.org/ac

Disentangling Dynamic Changes of Multiple Cellular Components during the Yeast Cell Cycle by *in Vivo* Multivariate Raman Imaging

Chuan-Keng Huang,[†] Masahiro Ando,[‡] Hiro-o Hamaguchi,[†,‡] and Shinsuke Shigeto*[,†]

[†]Department of Applied Chemistry and Institute of Molecular Science, National Chiao Tung University, Hsinchu 30010, Taiwan

[‡]Department of Chemistry, School of Science, The University of Tokyo, Tokyo 113-0033, Japan

Supporting Information

ABSTRACT: Cellular processes are intrinsically complex and dynamic, in which a myriad of cellular components including nucleic acids, proteins, membranes, and organelles are involved and undergo spatiotemporal changes. Label-free Raman imaging has proven powerful for studying such dynamic behaviors *in vivo* and at the molecular level. To construct Raman images, univariate data analysis has been commonly employed, but it cannot be free from uncertainties due to severely overlapped spectral information. Here, we demonstrate multivariate curve resolution analysis for time-lapse Raman imaging of a single dividing yeast cell. A four-dimensional (spectral variable, spatial positions in the two-dimensional image plane, and time sequence) Raman data "hypercube" is unfolded to a two-way array and then analyzed globally using multivariate curve resolution. The multivariate Raman imaging thus accomplished successfully disentangles dynamic changes of both concentrations and distributions of major cellular components (lipids, proteins, and polysaccharides) during the cell cycle of the yeast cell. The results show a drastic decrease in the amount of lipids by ∼50% after cell division and uncover a protein-associated component that has not been detected with previous univariate approaches.

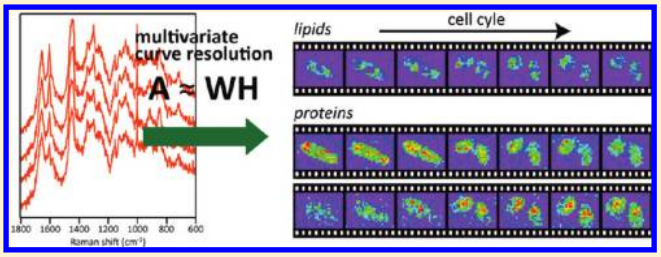

The cell cycle plays a pivotal role in reproduction of all living organisms. The molecular mechanisms of the cell cycle have been intensively studied over the last 40 years by genetic and molecular biological approaches using fission yeast and budding yeast as model organisms.[1,2] The cell cycle, like any other cellular processes, is highly dynamic in nature and its mechanistic study requires time and space specificity as well as chemical specificity. Among various microspectroscopic methods developed to date, Raman spectroscopy has emerged as a potential bioimaging tool to meet these requirements with nondestructive, less invasive, and label-free characteristics.[3−8]

We have very recently achieved the first multimode time-lapse Raman imaging of a single dividing *Schizosaccharomyces pombe* cell, in which Raman images for nine vibrational modes in the fingerprint region (800−1800 cm^{-1}) were obtained simultaneously at different cell-cycle stages of the *S. pombe* cell.[9] We showed that the concentrations and distributions of lipids and proteins varied in a concerted manner as the cell cycle proceeded. In that work, we used a univariate data analysis to construct Raman images. The univariate Raman image based on a single Raman band is readily obtained by integrating the Raman intensity under the band contour at each position in the image plane, followed by assembling these Raman intensities calculated at all positions to generate a two-dimensional (2D) map of the intensity distribution.[3,4,10] Because Raman intensity is proportional to the concentration of a molecular species that gives rise to the Raman band, the Raman image so obtained displays a relative concentration map of the molecular species.

Despite the simplicity of the principle, univariate Raman imaging often suffers from a limitation inherent to cellular vibrational spectra. The limitation arises from severely overlapped spectral information. An enormous variety of biomolecules can contribute to a cellular Raman spectrum and each of the biomolecules in turn exhibits many (broad) Raman bands, thus lowering chemical specificity. For example, the amide I band of proteins completely overlaps with the *cis*-C═C stretch band of unsaturated lipids, with both peaking at around 1655 cm^{-1}.[11] Therefore, the Raman image at 1655 cm^{-1} (see below) contains contributions from both lipids and proteins. This limitation indeed prevented us from fully utilizing the nine Raman images; only four of them that can be assigned unambiguously were discussed in detail.[9] Without careful consideration on band assignments, univariate Raman images could lead to erroneous interpretations of the underlying biochemistry.

Multivariate data analysis, such as principal component analysis[12−18] (PCA), cluster analysis,[6,13,14,18−20] and multivariate curve resolution[12,14,17,21,22] (MCR, also known as nonnegative matrix factorization[23,24]), is a more preferred approach, because it is capable of extracting maximum chemical information from complicated Raman spectra without a priori knowledge about spectral characteristics. In a multivariate data

Received: March 27, 2012
Accepted: May 31, 2012
Published: May 31, 2012

   dx.doi.org/10.1021/ac300834f | *Anal. Chem.* 2012, 84, 5661−5668

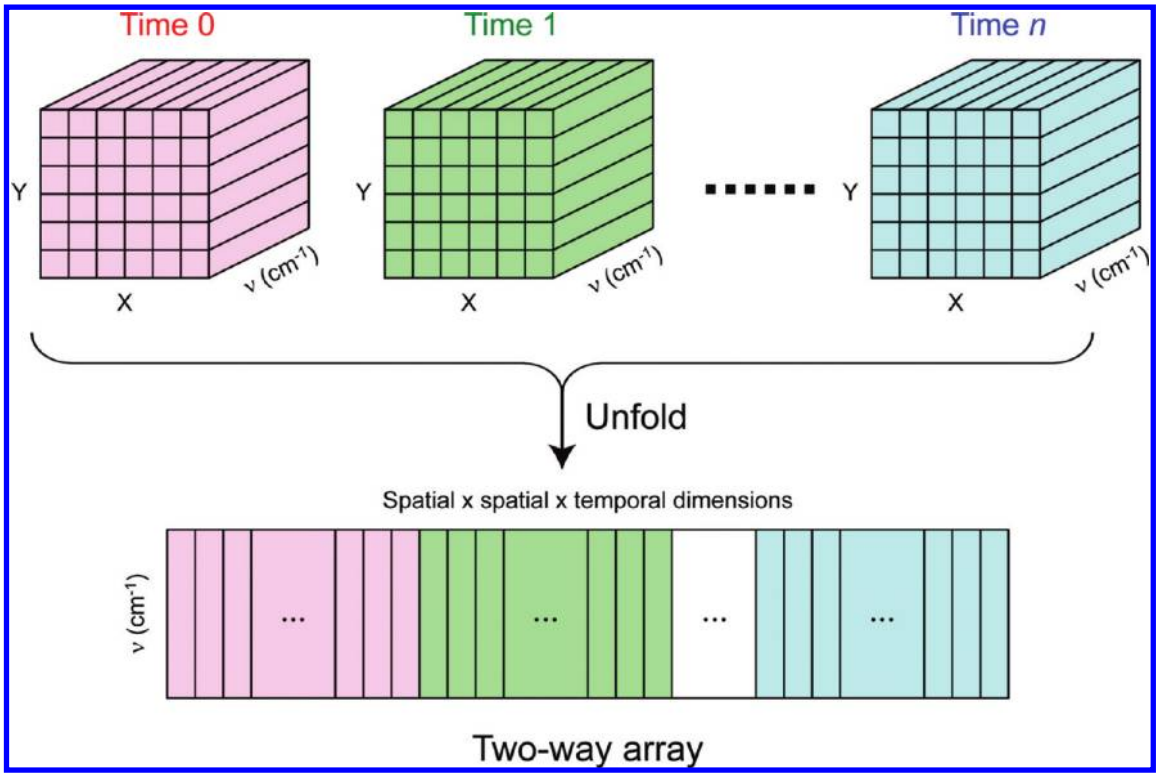

Figure 1. Diagrammatic representation of the unfolding of overall four-dimensional spectral data into a two-way array that facilitates multivariate data analysis. X and Y denote positions in the image plane, and ν denotes the spectral dimension. The three dimensions (two spatial and one temporal dimensions) are combined to be a single dimension. In the present study, the resulting matrix consisted of 790 rows and 6885 columns.

analysis, instead of mapping the intensity of an individual band, a whole set of spectral data are analyzed globally. As a result, the data are reduced to the intrinsic spectra of components present in the sample and their concentration profiles, which lend themselves to provide a holistic view of the original data. Applications of multivariate data analysis to Raman microspectroscopy and imaging are rapidly growing and include characterization of pharmaceutical samples,[14,16,17] living cell studies,[5,6,13,15] and so forth. However, the high potential of the multivariate approaches has not been fully exploited for understanding dynamic aspects of cellular processes including the cell cycle, at the single-cell level.

In this paper, we demonstrate the power of multivariate time-lapse Raman imaging of a single dividing *S. pombe* cell using MCR. This paper extends our previous work[9] through substantial advances in experimental conditions and through the use of multivariate data analysis. A laboratory-built high-sensitivity confocal Raman microspectrometer[8,9] is used to measure space-resolved Raman spectra at characteristic time points before, in the middle of, and after the cell division of the target *S. pombe* cell. MCR with a laboratory-developed software yields the intrinsic spectra and relative concentration distributions of three major constituents of the cell, namely, lipids, proteins, and polysaccharides. The total amount of lipids within the cell decreases drastically by ∼50% after the cell division. Intriguingly, two protein-associated components are found. One is the dominant contribution that accounts for most of the characteristic protein Raman bands and shows quite a similar time evolution to lipids, whereas the other, which has been detected for the first time by using MCR, shows a continuous increase with time. Biological implications of these resolved components and their dynamics as well as comparison with the univariate analysis are discussed.

EXPERIMENTAL SECTION

Cell Culture and Sample Preparation. *Schizosaccharomyces pombe*, a haploid yeast, was cultured in PMLU medium according to ref 25. *S. pombe* cells grew in the PMLU medium as well as in nutrient-rich YES medium (Figure S1, Supporting Information). The sample was housed in a laboratory-built chamber that enabled us to control the surrounding temperature and to keep humidity (Figure S2, Supporting Information). The use of this chamber prevented the medium from drying and provided better growing environments than in the previous work[9] with fresh air flow at 30 °C during the 22 h Raman imaging experiment.

Confocal Raman Microspectroscopy and Imaging. Time-lapse Raman imaging experiments were performed with a laboratory-built confocal Raman microspectrometer (Figure S3, Supporting Information), as described previously.[8,9] The 632.8 nm line of a He−Ne laser (1 mW at the sample point) was used as the Raman excitation light. The low excitation laser power was important to reduce photodamage as much as possible. Imaging experiments were performed at nine different times (1, 2, 4, 6, 6.5, 10, 14, 18, and 22 h after inoculation of yeast cells into PMLU medium) in the cell cycle. The sample housed in the chamber was translated in a raster manner by a piezoelectric nanopositioner with a 0.5 μm step in both the X and Y directions so that the laser spot scanned across the selected cell. At each position, the Raman spectrum was recorded with a 1.5 s exposure time, resulting in a time resolution of 15−20 min (1.5 s/pixel for 600−800 pixels depending on the image size). Lateral (XY) resolution was 0.5 μm, which was determined by

dx.doi.org/10.1021/ac300834f | *Anal. Chem.* 2012, 84, 5661−5668

the step used in imaging experiments rather than by the estimated optical resolution (0.3 μm). Axial (Z) resolution was 2.4 μm. Because the typical thickness of an *S. pombe* cell is ~2 μm, the effective focal volume contained the whole cell along the Z direction.

Data Analysis. Initially, Raman spectra recorded at N_{XY} positions in a 2D scan at a given measurement time constituted a three-dimensional (spectral × spatial × spatial dimensions) data cube. The value of N_{XY} was 609 (= 21 × 29) at 1 h, 690 (= 23 × 30) at 2 h, 713 (= 23 × 31) at 4 and 6 h, and 832 (= 26 × 32) at 6.5−22 h. The spectral window covering the fingerprint region was always set to be 790 pixels. The data was unfolded into a matrix with 790 rows and N_{XY} columns. Cosmic rays were manually removed if necessary, followed by a singular value decomposition (SVD) of the matrix to reduce noise.[8,9,26,27] After the data preprocessing, two approaches were employed to construct Raman images, namely, the univariate analysis and MCR.

In the univariate analysis, the intensity of the Raman band of interest was first obtained by calculating the area intensity between the band contour and a baseline connecting the two ends of an interval chosen to include the whole band. Curve fitting was not used for this purpose due to the low signal-to-noise ratio (S/N). The Raman intensities evaluated at each point were then combined to construct a Raman image. The same procedure was repeated for all measurement times.

In MCR, given an $m \times n$ non-negative data matrix $\mathbf{A}$, a low-rank approximation of the matrix $\mathbf{A}$ is sought for by solving the problem[28,29]

$$\mathbf{A} \approx \mathbf{WH} \tag{1}$$

with non-negativity constraints $\mathbf{W} \geq 0$ and $\mathbf{H} \geq 0$. In the present case, $\mathbf{W}$ is an $m \times k$ matrix whose columns represent spectra and $\mathbf{H}$ is a $k \times n$ matrix whose rows represent spatiotemporal concentration profiles. k is a parameter that must be set a priori by the user. In physical terms, k denotes the number of underlying constituents. Neither a too small nor too large value of k gives successful MCR results. Unlike other factorization methods such as SVD, MCR does not require column/row vectors of the factors $\mathbf{W}$ and $\mathbf{H}$ to be orthogonal to each other but only requires their non-negativity.[28] This results in the major advantage of MCR over SVD and PCA that it is prone to yield sparse, physically interpretable solutions. The optimal solutions of $\mathbf{W}$ and $\mathbf{H}$ are obtained by solving alternating least-squares[23] (ALS) problems of eq 1 so that the Frobenius norm $\|\mathbf{A} - \mathbf{WH}\|_F^2$ is minimized.

The MCR procedure adopted in this work encompassed the following steps: (i) Generate the data matrix $\mathbf{A}$ by merging all the variables into a single dimension except for the spectral variable. By doing so, the originally four-dimensional Raman data hypercube was unfolded into a 790 × 6885 matrix (Figure 1). (ii) Initialization: SVD-based initialization[30] was used to obtain initial guesses for $\mathbf{W}$ and $\mathbf{H}$. The number of components was set to be $k = 6$, which yielded the best resolution of polysaccharide, lipid, and protein components. (iii) ALS optimization of $\mathbf{W}$ and $\mathbf{H}$ with L1-norm regularization (lasso regression[31]). An L1 penalty term of $\alpha^2 = 0.0095$ was added to obtain sparser solutions as

$$(\mathbf{W}^T\mathbf{W} + \alpha^2\mathbf{E})\mathbf{H} = \mathbf{W}^T\mathbf{A} \tag{2}$$

$$(\mathbf{HH}^T + \alpha^2\mathbf{E})\mathbf{W} = \mathbf{HA}^T \tag{3}$$

where $\mathbf{E}$ is a $k \times k$ matrix all of whose elements are unity. (iv) Repeat step iii until convergence was achieved. The number of iteration was set to be 4000, ensuring that $\|\mathbf{A} - \mathbf{WH}\|_F^2$ eventually converged to a sufficiently small, constant value. Note that because of the iterative nature of the MCR algorithms, the initialization of $\mathbf{W}$ and $\mathbf{H}$ is a key step for successful MCR. In addition to the SVD-based initialization used in this work, several methods have been proposed,[29] such as random initialization and a spherical k-means clustering approach.[32] To test the dependence of the results on initialization methods, random initialization was also attempted but in vain. A plausible reason for the failure would be that the likelihood of falling into a local minimum is higher with random initialization methods.[30] The MCR was performed on a software (nmf-11, Pylone) developed at Tokyo specifically for spectral imaging applications.

RESULTS AND DISCUSSION

Cell Cycle of *S. pombe*. The *S. pombe* cell cycle consists of four different phases called the M (mitosis) phase, G_1 (gap-1) phase, S (synthesis) phase, and G_2 (gap-2) phase (Figure 2).

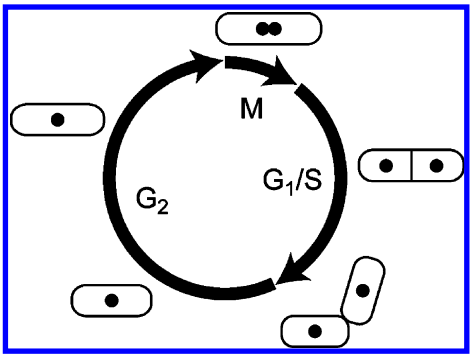

Figure 2. Schematic illustration of the *S. pombe* cell cycle. The oval bodies along the circle represent the morphology of cells in different phases. Dark spots represent the nuclei. Because *S. pombe* has a very brief G_1 phase, the notation G_1/S is used.

We randomly selected an *S. pombe* cell as the target that was in the G_2 phase. The morphological changes of the target cell captured by optical images (first column of Figure 3) tell us the cell-cycle stage at which each Raman imaging experiment was done. In the first four hours (1−4 h), the cell stays in the G_2 and M phases and prepares for a coming cell division, as evidenced by elongation of the cell by a factor of ~1.2 on going from 1 to 4 h. At 6 h, a septum is already formed to segregate the cell into two compartments, indicating that the cell is in the G_1/S phase. By 6.5 h, the cell division completes and the cell splits into two daughter cells. Subsequently, the daughter cells should enter a new cell cycle (G_2 phase again), but little morphological change is seen from 10 h up to 22 h. Although the cells apparently remain unchanged over the 10 h in terms of their morphology, molecular distributions within the cells probed by Raman imaging do vary with time as shown and discussed below.

Univariate Raman Images. The univariate data analysis yielded time-lapse Raman images of the dividing *S. pombe* cell for 10 Raman bands (Figure 3). The time dependence of the total relative concentrations of selected bands is shown in Figure 4. Previously we reported nine univariate Raman images at six different stages in the cell cycle.[9] The univariate Raman images and their temporal changes obtained in the present

dx.doi.org/10.1021/ac300834f | *Anal. Chem.* 2012, 84, 5661−5668

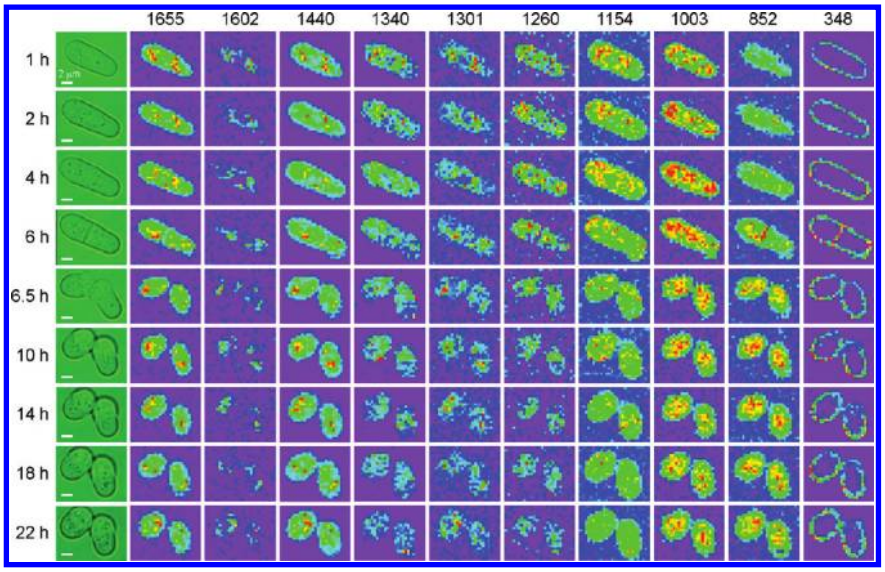

Figure 3. Time-lapse univariate Raman images of a single dividing *S. pombe* cell at the Raman shift of 1655, 1602, 1440, 1340, 1301, 1260, 1154, 1003, 852, and 348 cm^{-1} (from left to right), together with its optical images (first column). The Raman shift of each band is indicated at the top of the corresponding column of images. All images presented here have been cropped to the same size, i.e., 21 × 27 pixels (10.5 × 13.5 μm^2), for consistency. Scale bar = 2 μm.

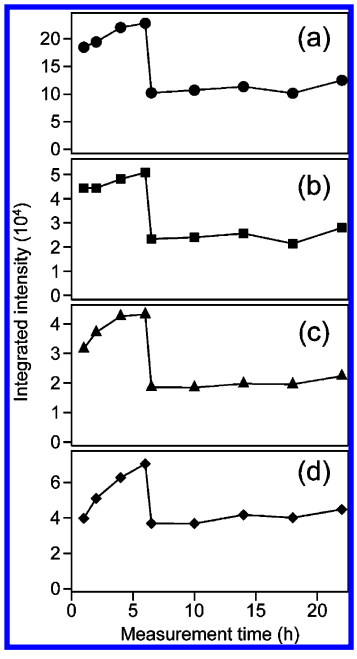

Figure 4. Time dependence of the Raman intensities at 1440 (a), 1301 (b), 1003 (c), and 852 (d) cm^{-1}, integrated over the whole cell. The 1440 and 1301 cm^{-1} bands are assigned to lipids and the 1003 and 852 cm^{-1} bands to proteins.

study agree well with those already reported by us. It is worth mentioning that improved S/N and sample conditions (see the Experimental Section) have allowed us to add the images of one more Raman band at 348 cm^{-1} (assigned to polysaccharides[33,34]) and three more measurement times, thereby providing more detailed information on the cell cycle dynamics.

With few exceptions, it is difficult to unambiguously assign the observed Raman bands to known biomolecules due to considerable spectral overlap. In addition to the amide I and C=C stretch region discussed above, the 1100−1400 cm^{-1} region is so crowded that the Raman images at 1340, 1260, and 1154 cm^{-1} more or less contain multiple contributions. The Raman band at 1602 cm^{-1} is relatively isolated from the others, but it has not yet been given a conclusive assignment.[35−37] To cope with this problem, we classified in the previous paper[9] the nine Raman images into three groups: Raman images of lipids, proteins, and admixtures of both and other molecular species. The same classification also works in the present case. However, it leaves only four Raman images (1440 and 1301 cm^{-1} for lipids and 1003 and 852 cm^{-1} for proteins), out of the 10, for discussion of their specific dynamic behaviors (Figure 4). To take full advantage of the rich information content contained in our Raman spectral data, we need to go beyond the univariate approach.

Multivariate Raman Images. The MCR analysis of the same data set as used for the univariate analysis derived time-lapse Raman images and component spectra of six chemical species (Figure 5). The six components are denoted 1−6. The vectors representing the spectra are normalized so that the sum of their components is equal to unity. To our knowledge, this is the first successful application of MCR analysis to Raman imaging of the cell cycle dynamics.

Before discussing each component in detail, we check the validity of the MCR analysis. To see how well the six components reproduce the original data, we plot the normalized residual matrix **R** (Figure 6a) calculated using the following equation:

$$R_{ij} = [A_{ij} - (WH)_{ij}]/A_{ij} \quad (4)$$

Besides vertical stripes indicating the locations of intense Raman bands, the 2D plot shows no particular distribution patterns and residues seem to be randomly distributed. As compared in Figure 6b, a typical preprocessed spectrum (after SVD denoising) and the corresponding MCR fitted spectrum look nearly identical; their difference spectrum shows fitting residue of less than 10%. Taken together, we confirm that the original image data is well reproduced by the six components through the present MCR analysis.

dx.doi.org/10.1021/ac300834f | *Anal. Chem.* 2012, 84, 5661−5668

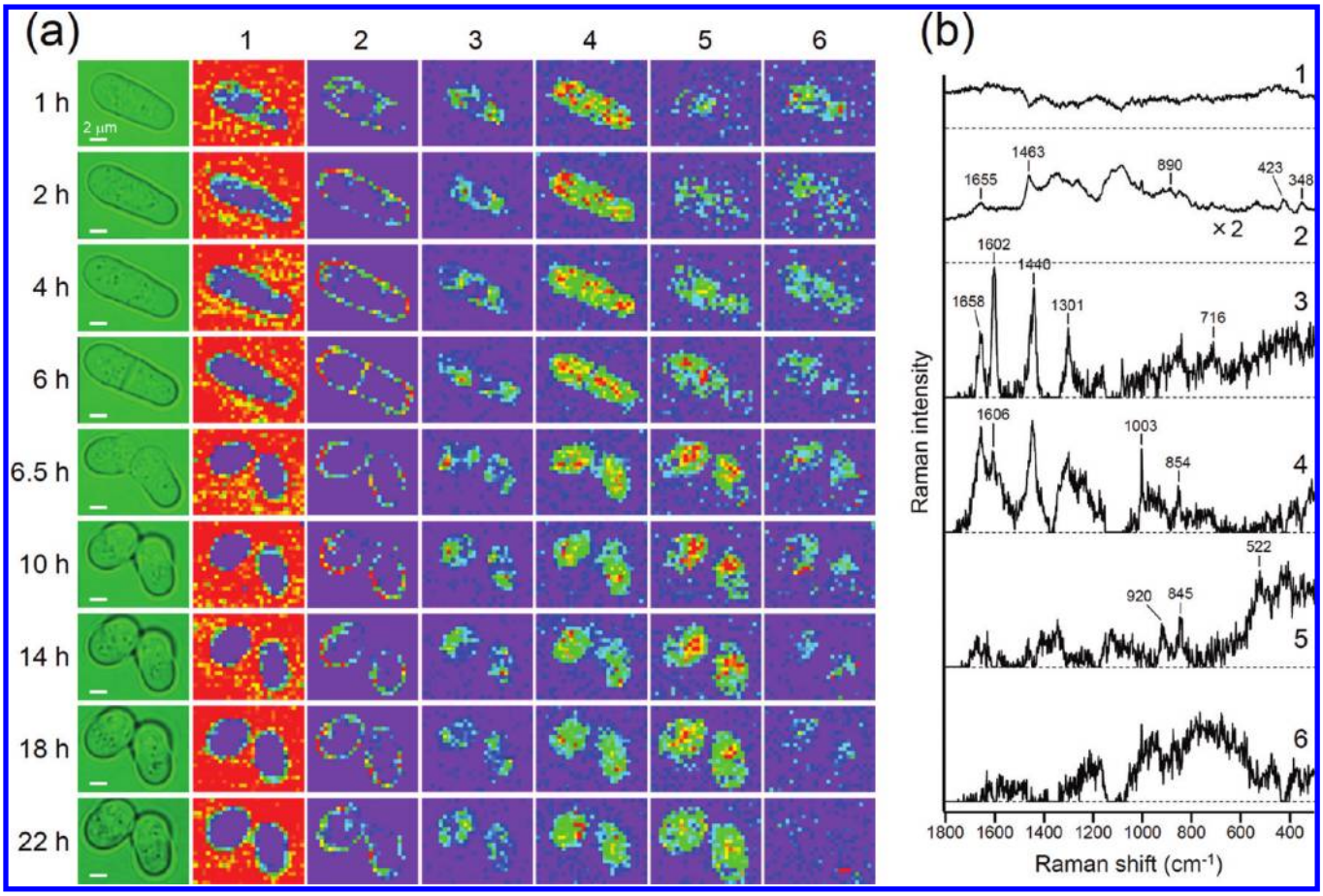

Figure 5. Time-lapse multivariate Raman imaging of the single dividing *S. pombe* cell. (a) Raman images of six components (1−6) derived from the MCR, together with the optical images (leftmost column). Scale bar = 2 μm. (b) Normalized Raman spectra of components 1−6. The spectra are displaced vertically for clarity with the zero line of each spectrum indicated by a dashed line.

Component 1 is associated with the background, because it exclusively shows red (high-intensity) distribution patterns outside the cell(s) (Figure 5a-1) and a featureless spectrum (Figure 5b-1). Component 2 can also be undoubtedly attributed to polysaccharides such as β-1,3-glucan, the major constituent of the yeast cell wall.[38] The Raman images of component 2 (Figure 5a-2) clearly visualize the cell wall at all measurement times and the septum at 6 h. Furthermore, the spectrum of component 2 (Figure 5b-2) is in good agreement with the reported Raman spectrum of β-1,3-glucan.[4] According to the normal-mode analysis of model disaccharides,[33,34] the low-frequency bands at 348 and 423 cm^{-1} are predominantly attributed to the skeltal deformations (C−C−C, C−C−O, and O−C−O), the 890 cm^{-1} band to the C−O stretch mode of the glycosidic linkage, and the 1463 cm^{-1} band to the CH bending mode of the CH_2OH group.

Component 3 is assigned to lipids. Although somewhat noisy, the spectrum of component 3 (Figure 5b-3) reproduces most of the bands found in the lipid-rich Raman spectrum, including those at 716, 1301, 1440, 1602, and 1658 cm^{-1}. In particular, the 716 cm^{-1} band is a characteristic spectral signature of the phospholipid headgroup.[39,40] Another support for the assignment comes from the time-lapse Raman images (Figure 5a-3). Close inspection of the distribution pattern of these images shows a blue (low-intensity) region around the center of the cell that corresponds to the nucleus. This result is consistent with a low concentration of lipids in nuclei. Furthermore, the time dependence of the Raman images of component 3 closely resembles that of the univariate Raman image at 1301 cm^{-1} (Figure 3), which is assigned to lipids.

Now that components 2 and 3 have been identified, respectively, as polysaccharides and lipids, it would be natural to attribute the remaining components 4 and 5 to spectra associated with proteins. We can justify our interpretation by their dynamics and spectral patterns. Concerning the dynamics, the multivariate Raman images of components 4 and 5 (Figure 5a-4,5) show a behavior similar to the univariate Raman images of protein bands at 1003 and 852 cm^{-1} (Figure 3), respectively. With regard to the spectral pattern, we synthesized the spectra of components 4 and 5 (Figure 5b-4,5) and found that the synthesized spectrum coincides well with the protein-rich Raman spectrum of the *S. pombe* cell.

First, let us look into the spectrum of component 4, the major protein component (Figure 5b-4). The ring breathing mode of phenylalanine residues at 1003 cm^{-1}, which is the most direct Raman indicator of proteins, is clearly observed. In addition to the 1003 cm^{-1} band, we see three prominent bands at 1658, 1606, and 854 cm^{-1}. The 1606 cm^{-1} band is also assigned to phenylalanine residues.[41] The 854 cm^{-1} band is one of the tyrosine doublet, which arises from a Fermi resonance between the ring breathing fundamental and the overtone of an out-of-plane ring bending vibration of tyrosine residues.[42] The counterpart of the doublet should appear around 830 cm^{-1}, but

dx.doi.org/10.1021/ac300834f | *Anal. Chem.* 2012, 84, 5661−5668

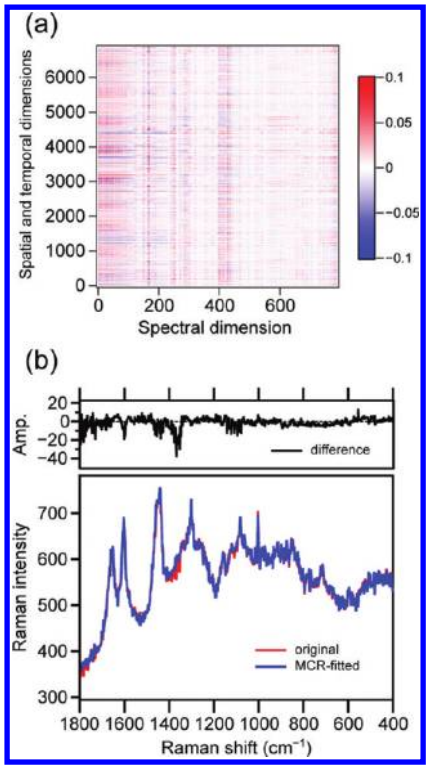

Figure 6. (a) 2D plot of the residual matrix **A** − **WH** (see eq 4 for definition). (b) Comparison of a typical SVD-treated Raman spectrum (red curve) and the corresponding MCR fitted spectrum (blue curve). Also shown is their difference spectrum (black curve; red curve minus blue curve).

it is probably too weak to be seen in the spectra of component 4 (Figure 5b-4) and component 5 (Figure 5b-5).

What then is component 5? We noticed the band at 845 cm^{-1} (Figure 5b-5). Previous Raman studies[43,44] show that the tyrosine doublet at about 854 and 830 cm^{-1} collapses to a single band appearing in between the doublet peaks upon phosphorylation of tyrosine residues. It is therefore plausible that the 845 cm^{-1} band observed in Figure 5b-5 is due to the collapsed band of the tyrosine doublet. It is also shown for some test peptides that a band emerges at ∼920 cm^{-1} upon tyrosine phosphorylation,[43] which is also observed in Figure 5b-5. The band at 522 cm^{-1} is likely attributable to the S−S stretch of disulfide bonds.[41] Both phosphorylation and formation of disulfide bridges are indicative of structural changes of proteins during the cell cycle of the *S. pombe* cell. It is tempting to think of component 5 alone as representing a specific class of proteins. However, spectral features characteristic of proteins such as the amide I band and the phenylalanine band at 1003 cm^{-1} are almost completely missing in the spectrum of component 5 (Figure 5b-5). The absence of these protein markers may result from a flaw in the present MCR analysis. The true spectrum of proteins that are associated with phosphorylation would be given by a linear combination of the spectra of components 4 and 5. Further insight into component 5 is provided by the time dependence of the relative concentration (see below).

The origin of component 6 is unclear. As seen from Figure 5a-6, its time-lapse Raman images look like those of lipids (component 3, Figure 5a-3), but its intrinsic spectrum (Figure 5b-6) shows no noticeable Raman features. In contrast with the other components, component 6 is not reproducible; the appearance of this component seems to depend on the data set. Therefore, we leave this component for further investigations and will not discuss it in the rest of this paper.

Time Dependence of Lipid and Protein Concentrations. We have assigned above the five components derived from the MCR according to their spectra and qualitative temporal changes of their Raman images. More quantitative insight should be gained from the time dependence of the relative concentration of each component. Figure 7 plots the

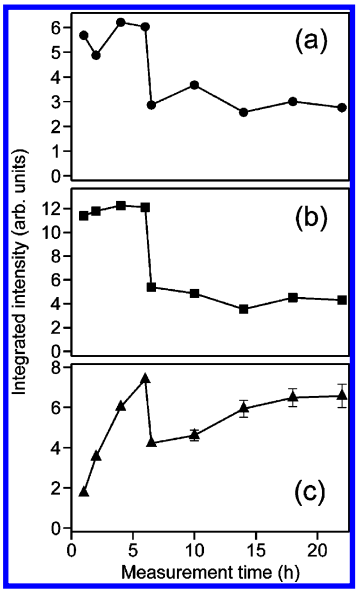

Figure 7. Time dependence of the Raman intensities integrated over the whole cell for components 3 (a, lipids), 4 (b, major protein component), and 5 (c). Error bars were obtained by taking into account uncertainties in the location of the cell wall. In parts a and b, error bars are smaller than symbols.

time dependence of the Raman intensities for lipids (component 3) and proteins (4 and 5) integrated over the whole cell (for 6.5−22 h, the left cell). We use the polysaccharide images (Figure 5a-2) to accurately know on the molecular basis the pixels giving the cell wall and sum up all the Raman intensities inside those pixels. Therefore, the integrated Raman intensity can be viewed as representing the total relative concentration of each component.

The total concentration of lipids (Figure 7a) does not change much before the cell divides. However, it suddenly drops by ∼50% at 6.5 h, when the cell splits into two daughter cells and remains constant for more than 15 h afterward. Such a drastic decrease of lipids soon after the formation of a septum has not so far been observed by any methods other than Raman spectroscopy. The total relative concentration of lipids estimated with our method has important biological implications, because it allows us to quantitatively discuss how much energy is stored[45] and used in the form of lipids before and after cell division. The result shown in Figure 7a may indicate that a lot of energy is consumed when the *S. pombe* cell divides. Similar dynamics are observed for the major protein component (Figure 7b).

Component 5 exhibits markedly different time dependence (Figure 7c) from the lipid and major protein components. This component increases very rapidly before the cell division; the intensity at 6 h is about 4 times as large as that at 1 h. The integrated intensity then decreases by ∼60%, analogous to the

dx.doi.org/10.1021/ac300834f | *Anal. Chem.* 2012, 84, 5661−5668

other two components. After the cell division, it again increases monotonically but with a slower rate.

The 522, 845, and 920 cm^{-1} bands observed in the spectrum of component 5 (Figure 5b-5) may look questionable because they are smaller in intensity than a broad feature in the low-frequency region of the same spectrum. However, we can also see those Raman bands in averaged raw Raman spectra without performing MCR. Figure 8 shows a time lapse of space-resolved

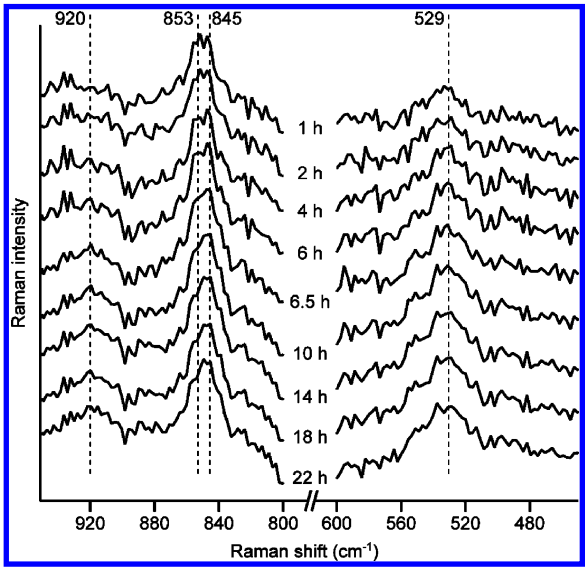

Figure 8. Time-lapse raw Raman spectra of the *S. pombe* cell. Each spectrum is an average of eight spectra that were recorded around the center of the cell, where the intensity of component 5 is strong (see Figure 5a-5).

Raman spectra, each of which is an average of eight spectra that were obtained around the center of the *S. pombe* cell. Consistent with Figure 7c, the three bands at ~529, 845, and 920 cm^{-1} in Figure 8 do increase with time, confirming the validity of the MCR analysis.

On the basis of primarily the spectrum (Figure 5b-5), we have conjectured that component 5 is attributed at least partially to protein molecules that undergo chemical modifications such as phosphorylation during the cell cycle. Given that protein phosphorylation plays an important role in numerous cellular processes including the cell cycle[46] and DNA repair,[47,48] this interpretation sounds plausible. The continuous increase of component 5 (Figure 7c), however, also suggests another important possibility that component 5 is somehow related to the effects of laser irradiation. It is known that the expression of a class of proteins known as heat shock proteins is significantly increased when cells are exposed to external stress such as elevated temperature. Although our excitation wavelength (632.8 nm) lies very close to a biological window (660–850 nm), the temperature of a laser-irradiated cell could be locally high and put certain stress on it. The unusually slow cell cycle observed in our experiment may be a consequence of the stress. Biochemical studies together with Raman microspectroscopy are needed to clarify this issue. Nevertheless we underline here that although the MCR presents limitations in separating proteins as discussed above, it was not until we performed the MCR that such a characteristic protein-associated component was extracted from complicated Raman images.

Comparison between the Univariate and Multivariate Approaches. In this section, we compare the two approaches in terms of their merits and drawbacks and discuss possible improvements in the MCR algorithm. The greatest advantage of the univariate approach lies in its simplicity.[16] It is straightforward to perform, and yet it gives results that are in reasonable agreement with those obtained with the MCR. However, univariate Raman images often overestimate the band intensity of a molecular species due to overlapping bands of other species. To see this, compare, for example, the univariate Raman images at 1440 cm^{-1} (Figure 3) and the multivariate Raman images of lipids (Figure 5a-3). Compared with the multivariate images, the univariate images display green (moderate-intensity) patterns that spread over the entire cell.

In contrast to the univariate method, we are able to choose the optimal multivariate method among various options. Miljković et al.[18] have made a detailed comparison of the contrast of Raman images obtained with five established multivariate methods and illustrated which method provides the best contrast hinges on the variance in the data set. If the data set contains large spectral differences, such as those manifested by isotope-substituted component spectra, the component can be readily resolved even in the presence of a large noise. Likewise, incorporation of temporal information in multivariate analysis is of great help with this regard. In the present study, component 5 has been differentiated from the others partly because of its unique time evolution (see Figure 7a–c).

A few dips and many zero-filled regions are found in the component spectra we obtained with the MCR (Figure 5b). These are physically unreasonable and need to be removed by, e.g., introducing additional penalty term to eqs 2 and 3 on the basis of the second derivatives of the spectra. The regularization terms can also be extended to take into account spatial correlation between nearby positions in the image data and/or spectral correlation. All these penalizations will improve results of MCR analysis in terms of their physical interpretability, but the calculations are computationally highly demanding and are not practically feasible when the data is very large.

■ CONCLUSIONS

We have demonstrated a thorough analysis of time-lapse Raman images of a single dividing *S. pombe* cell with the use of the MCR method. Our approach with MCR requires minimum user interaction and offers a robust platform for molecular-level analysis of cellular dynamics. Only a few steps of preprocessing and data reorganization are required. Owing to non-negativity constrains imposed in MCR, there is in general no need to take linear combinations of the decomposed vectors. The method does not demand detailed spectral characterization, so it can be deployed in other types of cells that have not been as well understood as yeast cells. Therefore, we believe that label-free Raman imaging combined with MCR should be added to the toolbox for single-cell analysis with high chemical specificity.

■ ASSOCIATED CONTENT

Ⓢ Supporting Information

Additional information as noted in text. This material is available free of charge via the Internet at http://pubs.acs.org.

AUTHOR INFORMATION

Corresponding Author

*E-mail: shigeto@mail.nctu.edu.tw.

Notes

The authors declare no competing financial interest.

ACKNOWLEDGMENTS

The authors thank Mr. Hirokazu Minami (Pylone) for his collaboration in the development of the MCR software. S.S. and H.-o.H. were supported by National Chiao Tung University and the Ministry of Education, Taiwan ("Aiming for the Top University" plan). H-o.H. was supported by the Science and Technology Agency of Japan (JST). S.S. was supported in part by the National Science Council of Taiwan Grant NSC100-2113-M-009-009-MY2.

REFERENCES

(1) Hartwell, L. H. *Bacteriol. Rev.* **1974**, *38*, 164−198.
(2) Forsburg, S. L.; Nurse, P. *Annu. Rev. Cell Biol.* **1991**, *7*, 227−256.
(3) van Manen, H.-J.; Uzunbajakava, N.; van Bruggen, R.; Roos, D.; Otto, C. *J. Am. Chem. Soc.* **2003**, *125*, 12112−12113.
(4) Huang, Y.-S.; Karashima, T.; Yamamoto, M.; Hamaguchi, H. *Biochemistry* **2005**, *44*, 10009−10019.
(5) Matthäus, C.; Boydston-White, S.; Miljković, M.; Romeo, M.; Diem, M. *Appl. Spectrosc.* **2006**, *60*, 1−8.
(6) van Manen, H.-J.; Lenferink, A.; Otto, C. *Anal. Chem.* **2008**, *80*, 9576−9582.
(7) Ogawa, M.; Harada, Y.; Yamaoka, Y.; Fujita, K.; Yaku, H.; Takamatsu, T. *Biochem. Biophys. Res. Commun.* **2009**, *382*, 370−374.
(8) Noothalapati Venkata, H. N.; Nomura, N.; Shigeto, S. *J. Raman Spectrosc.* **2011**, *42*, 1913−1915.
(9) Huang, C.-K.; Hamaguchi, H.; Shigeto, S. *Chem. Commun.* **2011**, *47*, 9423−9425.
(10) Naito, Y.; Toh-e, A.; Hamaguchi, H. *J. Raman Spectrosc.* **2005**, *36*, 837−839.
(11) Carey, P. R. *Biochemical Applications of Raman and Resonance Raman Spectroscopies*; Academic Press: New York, 1982.
(12) Shafer-Peltier, K. E.; Haka, A. S.; Motz, J. T.; Fitzmaurice, M.; Dasari, R. R.; Feld, M. S. *J. Cell. Biochem. Suppl.* **2002**, *39*, 125−137.
(13) Huang, W. E.; Griffiths, R. I.; Thompson, I. P.; Bailey, M. J.; Whiteley, A. S. *Anal. Chem.* **2004**, *76*, 4452−4458.
(14) Zhang, L.; Henson, M. J.; Sekulic, S. S. *Anal. Chim. Acta* **2005**, *545*, 262−278.
(15) Swain, R. J.; Jell, G.; Steves, M. M. *J. Cell. Biochem.* **2008**, *104*, 1427−1438.
(16) Šašić, S.; Clark, D. A.; Mitchell, J. C.; Snowden, M. J. *Analyst* **2004**, *129*, 1001−1007.
(17) Shinzawa, H.; Awa, K.; Kanematsu, W.; Ozaki, Y. *J. Raman Spectrosc.* **2009**, *40*, 1720−1725.
(18) Miljković, M.; Chernenko, T.; Romeo, M. J.; Bird, B.; Matthäus, C.; Diem, M. *Analyst* **2010**, *135*, 2002−2013.
(19) Mansfield, J. R.; Sowa, M. G.; Scarth, G. B.; Somorjai, R. L.; Mantsch, H. H. *Anal. Chem.* **1997**, *69*, 3370−3374.
(20) van Manen, H.-J.; Kraan, Y. M.; Roos, D.; Otto, C. *Proc. Natl. Acad. Sci. U.S.A.* **2005**, *102*, 10159−10164.
(21) Andrew, J. J.; Hancewicz, T. M. *Appl. Spectrosc.* **1998**, *52*, 797−807.
(22) de Juan, A.; Tauler, R. *Anal. Chim. Acta* **2003**, *500*, 195−210.
(23) Paatero, P.; Tapper, U. *Environmetrics* **1994**, *5*, 111−126.
(24) Lee, D. D.; Seung, H. S. *Nature* **1999**, *401*, 788−791.
(25) Moreno, S.; Klar, A.; Nurse, P. *Methods Enzymol.* **1991**, *194*, 795−823.
(26) Uzunbajakava, N.; Lenferink, A.; Kraan, Y.; Volokhina, E.; Vrensen, G.; Greve, J.; Otto, C. *Biophys. J.* **2003**, *84*, 3968−3981.
(27) van Manen, H.-J.; Kraan, Y. M.; Roos, D.; Otto, C. *J. Phys. Chem. B* **2004**, *108*, 18762−18771.
(28) Albright, R.; Cox, J.; Duling, D.; Langville, A. N.; Meyer, C. D. *NCSU Tech. Rep. Math* **2006**, 81706.
(29) Berry, M. W.; Brownea, M.; Langville, A. N.; Paucac, V. P.; Plemmons, R. J. *Comput. Stat. Data Anal.* **2007**, *52*, 155−173.
(30) Boutsidis, C.; Gallopoulos, E. *Pattern Recogn.* **2008**, *41*, 1350−1362.
(31) Tibshirani, R. *J. R. Stat. Soc. B* **2011**, *73*, 273−282.
(32) Wild, S.; Curry, J.; Dougherty, A. *Pattern Recogn.* **2004**, *37*, 2217−2232.
(33) Dauchez, M.; Derreumaux, P.; Lagant, P.; Vergoten, G.; Sekkal, M.; Legrand, P. *Spectrochim. Acta* **1994**, *50A*, 87−104.
(34) Dauchez, M.; Lagant, P.; Derreumaux, P.; Vergoten, G.; Sekkal, M.; Sombret, B. *Spectrochim. Acta* **1994**, *50A*, 105−118.
(35) Huang, Y.-S.; Karashima, T.; Yamamoto, M.; Ogura, T.; Hamaguchi, H. *J. Raman Spectrosc.* **2004**, *35*, 525−526.
(36) Onogi, C.; Torii, H.; Hamaguchi, H. *Chem. Lett.* **2009**, *38*, 898−899.
(37) Chiu, L.-d.; Hamaguchi, H. *J. Biophoton.* **2011**, *4*, 30−33.
(38) Northcote, D. H.; Horne, R. W. *Biochem. J.* **1952**, *51*, 232−236.
(39) Gaber, B. P.; Peticolas, W. L. *Biochim. Biophys. Acta* **1977**, *465*, 260−274.
(40) Akutsu, H. *Biochemistry* **1981**, *20*, 7359−7366.
(41) Naumann, D. *Appl. Spectrosc. Rev.* **2001**, *36*, 239−298.
(42) Siamwiza, M. N.; Lord, R. C.; Chen, M. C.; Takamatsu, T.; Harada, I.; Matsuura, H.; Shimanouchi, T. *Biochemistry* **1975**, *14*, 4870−4876.
(43) Moger, J.; Gribbon, P.; Sewing, A.; Winlove, C. P. *Biochim. Biophys. Acta* **2007**, *1770*, 912−918.
(44) Xie, Y.; Zhang, D.; Jarori, G. K.; Davisson, V. J.; Ben-Amotz, D. *Anal. Biochem.* **2004**, *332*, 116−121.
(45) Sorger, D.; Daum, G. *Appl. Microbiol. Biotechnol.* **2003**, *61*, 289−299.
(46) Maller, J. L. *Mol. Cell. Biochem.* **1993**, *127*, 267−281.
(47) Flott, S.; Alabert, C.; Toh, G. W.; Toth, R.; Sugawara, N.; Campbell, D. G.; Haber, J. E.; Pasero, P.; Rouse, J. *Mol. Cell. Biol.* **2007**, *27*, 6433−6445.
(48) Flott, S.; Rouse, J. *Biochem. J.* **2005**, *391*, 325−333.